CrossMark

ORIGINAL PAPER

Structural, vibrational and thermophysical properties of pyrophyllite by semi-empirical density functional modelling

Gianfranco Ulian[1] · Giovanni Valdrè[1]

Abstract Pyrophyllite has a significant role in both geophysics as a hydrous phase, which can recycle water into the Earth's mantle, and many industrial applications, such as petroleum and civil engineering. However, very few works have been proposed to fully characterize the thermodynamic properties of this mineral, especially at atomic scale. In the present work, we report structural, vibrational, thermochemical and thermophysical properties of pyrophyllite, calculated at the density functional theory level with the hybrid B3LYP functional, all-electron Gaussian-type orbitals and taking into account a correction to include dispersive forces. $V(P, T)$ data at 300 K fit with isothermal third-order Birch–Murnaghan equations of state and yield $K_{T0} = 46.57$ GPa, $K' = 10.51$ and $V_0 = 213.67$ Å^3, where K_{T0} is the thermal bulk modulus at 0 GPa, K' is the first derivative and V_0 is the volume at zero pressure, in very good agreement with recent experimental results obtained by in situ single-crystal synchrotron XRD. The compressional behaviour is highly anisotropic, with axial compressibility in ratio $\beta(a):\beta(b):\beta(c) = 1.218:1.000:4.188$. Pyrophyllite bulk modulus, thermal expansion coefficients and heat capacity at different $P–T$ conditions are provided. The results of this kind of analysis can be useful in both geophysical and technological applications of the mineral and expand the high-temperature and high-pressure knowledge of this phase at physical conditions that are still difficult to obtain by experimental means. The simulated vibrational spectrum can also be used as a guideline by other authors in their experimental investigation of pyrophyllite.

Introduction

Pyrophyllite (ideally [$Al_2Si_4O_{10}(OH)_2$]) is the dioctahedral term of the phyllosilicate group consisting of simple 2:1 tetrahedral–octahedral–tetrahedral layers, namely TOT (Bruno et al. 2006; Evans and Guggenheim 1988). As shown in Fig. 1, the tetrahedral sheet is composed by individual SiO_4 tetrahedra linked by sharing three oxygen atoms (basal oxygen, O^b) with SiO_4 neighbours to form infinite two-dimensional sheets with a hexagonal-based patterns of linked sixfold rings; the plane formed by the basal oxygen is usually named "siloxanic basal plane". The fourth corner (apical oxygen, O^a) does not link to other tetrahedral groups, but it is shared with the underneath Al octahedron. The octahedrally coordinated cations form a sheet, in which individual polyhedra are laterally linked by edge sharing. In pyrophyllite, only 2/3 of the octahedral sites are occupied mainly by aluminium. The 2:1 layer is composed of two opposing tetrahedral sheets with the octahedral sheet in between (see Fig. 1). Since the TOT layer is electrically neutral, no interlayer cations exist in these structures and van der Waals forces hold them together. This leads to the extreme softness of the mineral along a direction perpendicular to the TOT layers. Pyrophyllite is commonly found in nature in three polytypic forms: a two-layer monoclinic (2 M), a one-layer triclinic (1Tc) and a disordered form (Evans and Guggenheim 1988). The crystal structure of pyrophyllite-1Tc was determined by different single-crystal X-ray diffraction

✉ Giovanni Valdrè
giovanni.valdre@unibo.it

[1] Dipartimento di Scienze Biologiche, Geologiche e Ambientali, Università degli Studi di Bologna, Piazza di Porta San Donato 1, 40126 Bologna, Italy
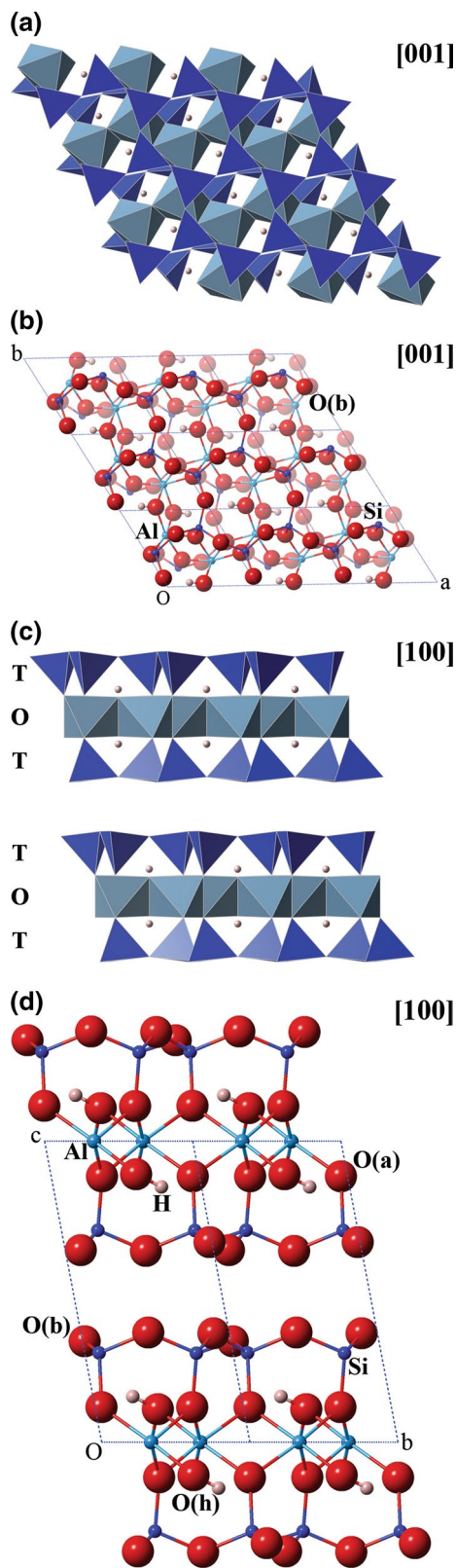
Fig. 1 Polyhedral models of the primitive cell of pyrophyllite as seen from the [010] and [001] directions. *Stick* and *ball* representation along the [100] direction was reported to clearly show the atomic arrangement

(XRD) refinements (Lee and Guggenheim 1981; Wardle and Brindley 1972).

From the geological point of view, pyrophyllite is one of the hydrous phases that in the last years has drawn a considerable interest in its high-pressure stability. Experimental studies have shown that some hydrous metamorphic minerals are stable to much greater depths in the Earth than previously evaluated (Pawley et al. 2002). Also, it seems that a range of new hydrous phases can be synthesized up to very high pressures. The attention to these minerals is mainly devoted to the processes in subduction zones, where dehydration is responsible for explosive volcanism and earthquakes (Grove et al. 2012; Sobolev and Chaussidon 1996). In this perspective, the high-pressure stability of hydrous phases determines the depth to which water can be recycled into the Earth's mantle and the amount of recycling that can take place.

Furthermore, pyrophyllite has been studied for its utilization in whiteware body as a replacement of quartz, clay or feldspar (Alimdzhanova et al. 1999; Bhasin et al. 2003; Lintz 1938) and for its significant role in many industrial applications, such as petroleum and civil engineering, food and cosmetic industry, heterogeneous catalysis and waste storage (Mazo et al. 2008). However, its use as a ceramic raw material is not yet widely accepted, probably because pyrophyllite seldom occurs in pure state like other silicates, such as kaolinite, and the presence of associated minerals (quartz, kyanite, sericite, diaspore) in the aggregated structure can influence its properties. There is still little information regarding thermomechanical transformation of pyrophyllite, which could be of upmost importance due to depleting resources of standard alumino-silicate minerals. In this prospective, few works have been recently conducted on both pure pyrophyllite and pired-pyrophyllite for its utilization in ceramic and porcelain systems (Mukhopadhyay et al. 2010, 2011).

One of the most important thermodynamic parameters of a mineral is its equation of state (EOS), i.e. the pressure and temperature dependence of its unit-cell volume. This is essential for calculating the $P–T$ conditions of mineral reactions. However, despite the importance of pyrophyllite in the water transport process in the Earth's mantle or industrial applications, very few works have been proposed to fully characterize the thermodynamic properties of this mineral phase. Furthermore, the results presented in literature are quite conflicting and far from modern standards.

A set of thermomechanical data for stoichiometric pyrophyllite was reported by Holland and Powell (1998), by deriving thermodynamic properties from equilibria involving pure end-members. The bulk modulus estimated at zero pressure and at 298 K (K_{T0}) by a Murnaghan equation of state fit (Murnaghan 1937) is 77 GPa, but its pressure derivative (K') was kept fixed at four during the fitting

procedure. With K_{T0} we indicate the bulk moduli at 0 GPa at specific temperature.

Pawley et al. (2002) measured the structural changes of pyrophyllite following a $P–T$ path in a range of pressure from 0 to 6.8 GPa between 300 and 700 K using a X-ray powder diffractometer equipped with a multi-anvil apparatus. The authors measured a powdered sample with NaCl as internal pressure standard. The data were fitted with a Murnaghan equation to obtain $K_{T0} = 37$ GPa and $K' = 10$. However, the authors did not make any high-temperature measurements at low pressure on pyrophyllite, which limited the possibility to determine the thermal expansivity (α_T) of the mineral and the thermal dependence of the bulk modulus ($\partial K_T/\partial T$). Very recently, Gatta et al. (2014) investigated the thermal and compressional behaviours of pyrophyllite by in situ synchrotron diffraction from 298 to 773 K (at 0.0001 GPa) and up to 6.2 GPa (at 298 K). The compressional results at room temperature were fitted with a third-order Birch–Murnaghan equation of state, with parameters $K_{T0} = 47(4)$ GPa and $K' = 7.3(19)$. The authors calculated the volume thermal expansion coefficient between 298 and 773 K, obtaining $\alpha_T = 2.2(2) \times 10^{-5}$ K^{-1} (reference temperature $T = 298$ K). As also mentioned elsewhere (Ulian et al. 2014), thermomechanical data of phyllosilicates tend to be highly dependent on the chemical composition and on the physical aspects of the samples (single crystals or powders), which explains the variability of the results presented in literature.

Nowadays, the interpretation of both diffraction and thermodynamic properties of complex mineral phases, such as phyllosilicates, has been facilitated by a class of independent, first-principles (sometimes termed "ab initio") quantum mechanical simulations. Regarding pyrophyllite, to our knowledge there is only one study aimed to obtain the elastic behaviour of this mineral (Voora et al. 2011). This work reported an interesting comparison between different density functional theory (DFT) methods, using plane-wave basis set, employed in the analysis of the mechanical behaviour of pyrophyllite. The theoretical bulk modulus and its first P derivative are in the ranges 38–41 GPa and 11–12, respectively, depending on the adopted DFT functional. The authors observed a better agreement with experimental mechanical results when using a semi-empirical correction for dispersive forces (Grimme 2006). In fact, while DFT-based approaches provide an adequate prediction of covalent bonding, they have a well-documented problem in describing long-range dispersion, which is often the driving force in weak interactions. For this reason, when dealing with weakly bound systems, such as layered minerals, it is recommendable to profit of some semi-empiric correction scheme, such as the DFT + D proposed by Grimme (2006). Recent works on talc, the trioctahedral phyllosilicate end-member, and

$2M_1$ muscovite, the potassium end-member of dioctahedral micas, proved the importance of this correction, which yields solid structural, chemical and physical results (Ulian et al. 2013, 2014; Ulian and Valdrè 2014a, b). However, the theoretical results of Voora et al. (2011) are related only to athermal condition, as they did not include the temperature as a variable.

To extend the investigation, in the present work we calculated the thermomechanical and thermochemical properties of pyrophyllite between 0 and 10 GPa and 10–900 K using a quantum mechanical approach based on the density functional theory (DFT) corrected for the dispersive forces, including the thermal effects by the quasi-harmonic approximation (Anderson 1995; Ulian and Valdrè 2014b). Furthermore, we have calculated and reported vibrational data of pyrophyllite, which can be useful for infrared/Raman analysis, an interpretation. Differently from the work of Voora et al. (2011), we used an all-electron localized Gaussian-type orbitals (GTO) and the B3LYP hybrid functional integrated with dispersive forces contribution. We have shown in previous works on talc mineral that this combination provides more accurate energy results than plane-wave simulations (Ulian et al. 2013, 2014). Starting from the XRD data of Lee and Guggenheim (1981), we optimized the pyrophyllite unit cell and internal geometry, and then, we investigated the vibrational and mechanical properties of the mineral. First, in order to gain information on the compressional behaviour of a pure pyrophyllite model, we analysed its structure from 0 to 10 GPa. A small range of negative pressures was also considered to explore the mineral behaviour under the effect of a hydrostatic tensile stress. These data were used to predict the equation of state, lattice and internal structural parameters of pyrophyllite at different temperatures (between 10 and 900 K) and were compared with previous theoretical and experimental results.

We reported three-dimensional plots of thermochemical results. The data can be useful to understand both the metamorphic and igneous equilibriums, and industrial applications of the mineral. Thermochemical results are compared with differential scanning calorimetry data obtained by Robie et al. (1976) and by Krupka et al. (1979).

Computational details

The calculations presented in this work have been performed with the ab initio CRYSTAL09 code (Dovesi et al. 2009), which implements the Hartree–Fock and Kohn–Sham self-consistent field method for the study of periodic systems. The graphical drawings have been carried out with the molecular graphics software VESTA (Momma and Izumi 2008).

Model structures

We modelled the pyrophyllite structure starting from XRD refinement data reported in literature (Lee and Guggenheim 1981), in the space group $P\bar{1}$. Oxygen atoms are subdivided in three groups: apical [O^a or O(a)] shared between Si and Al; hydroxyl [O^h or O(h)]; and basal [O^b or O(b)] shared between silica tetrahedrons. Since hydrogen atoms location has not been characterized by crystallographic studies, we initially considered two models where the O–H bonds were oriented parallel and perpendicular to the [001] direction. Then, we performed a free, non-constrained geometry optimization of the two structures, and in each case, we found a reasonable minimum with the O–H bond direction canted by about 60° with respect to the [001] direction. The stick and ball model in Fig. 1 shows a graphical representation of the mineral unit cell.

Hamiltonian and other parameters

We employed for the simulations the hybrid exchange functional B3LYP, which is the combination of the Becke three-parameter functional (Becke 1993) and the gradient-corrected correlation functional of Lee et al. (1988). The exchange–correlation contribution was calculated over a grid of 75 points and 974 angular points, obtained from the Gauss–Legendre quadrature and Lebedev schemes (Prencipe et al. 2004). This represents a good compromise between accuracy and cost of calculation for geometry optimization and vibrational frequencies. The values of the tolerances that control the truncation criteria for the bielectronic Kohn–Sham integrals were set to 10^{-6} and the pseudo-overlap parameter to 10^{-14}. This choice allows stabilizing the self-consistent behaviour during unit-cell deformations. The Hamiltonian matrix has been diagonalized through the Monkhorst and Pack (1976) scheme, using a $4 \times 4 \times 4$ k mesh, which leads to 36 reciprocal lattice points (k points). We chose this sampling grid to perform a better sampling along the **c** axis direction, due to the dispersive forces acting in that direction.

We adopted atomic Gaussian-type orbital (GTO) basis sets to describe the multi-electron wave functions. Some of them, namely those of silicon (88-31G*), oxygen (8-411d11G) and hydrogen (3-1p1), were used by some of us in our previous works on talc (Ulian et al. 2013, 2014; Ulian and Valdrè 2014b), since it presents a similar structure compared to pyrophyllite. The chosen basis sets, in particular one of the hydrogen atoms, allow accurate calculations in both molecular and crystal structures without too high computational costs. Aluminium atoms are described by a 8-511d1G basis set, which was optimized and used by Catti et al. (1994) to investigate corundum.

Lattice constants and internal coordinates were optimized within the same run using the analytical gradient

method for the atomic positions and a numerical gradient for the unit-cell parameters. The Hessian matrix was upgraded after each cycle with the Broyden–Fletcher–Goldfarb–Shanno algorithm (Broyden 1970a, b; Fletcher 1970; Goldfarb 1970; Shanno 1970). The geometry was considered converged when the tolerances for the maximum allowed gradient and the maximum atomic displacement were below 6×10^{-5} hartree bohr^{-1} and 1.2×10^{-5} bohr, respectively.

Generalized gradient approximation functionals and their hybrid forms, such as B3LYP, do not provide an adequate description of long-range dispersive interactions. Then, we evaluated dispersive forces according to the semi-empirical scheme (DFT + D) suggested by Grimme (2006), which adds the following contribution to the calculated DFT energy:

$$E_{\mathrm{DISP}} = -s_6 \sum_{\mathbf{g}} \sum_{i \neq j} f_{\mathrm{dump}} \left(R_{ij,\mathbf{g}}^6 \right) \frac{C_6^i C_6^j}{R_{ij,\mathbf{g}}^6} \qquad (1)$$

$$f_{\mathrm{dump}} = \frac{1}{1 + e^{-d(R_{ij,\mathbf{g}}/R_{vdw}-1)}}$$

The summation over all atom pairs ij and $\mathbf{g}$ lattice vectors exclude the self-interaction contribution ($i = j$) for every $\mathbf{g}$. The parameters C_6^i represent the dispersion coefficient for the atom i, $R_{ij,\mathbf{g}}$ is the interatomic distance between atom i in the reference cell and atom j in the neighbouring cells at distance $|\mathbf{g}|$ and s_6 is a functional-dependent scaling factor. We employed the C_6^i parameters reported in the work of Grimme (2006), which were obtained from atomic ionization potentials (I_p) and static dipole polarizabilities (α) according to the formula $C_6^i = 0.05 N I_p^i \alpha^i$, where N depends on atom row in the periodic table. The function f_{dump} is used to dump the energy correction to avoid double counting of short-range contributions and depends on the sum of atomic van der Waals radii (R_{vdw}) and on a steepness parameter ($d = 20$). Due to the molecular nature of the E_{DISP} correction, which tends to overestimate cohesive energy in solid crystals, the original B3LYP + D parameters were modified according to a previous study (Civalleri et al. 2008), setting s_6 to 1 and R_{vdw}(H) to 1.30, and the heavier atom van der Waals radii were scaled by a factor 1.05 (method called B3LYP-D*). The same approach has been adopted with good results in our previous works on talc (Ulian et al. 2013, 2014; Ulian and Valdrè 2014a, b).

Vibrational features

In periodic systems and within the harmonic approximation, the phonon frequencies at Γ point are evaluated by diagonalization of the central zone ($k = 0$) mass-weighted Hessian matrix:

$$W_{ij}(k=0) = \sum_G \frac{H_{ij}^{0G}}{\sqrt{M_i M_j}} \qquad (2)$$

H_{ij}^{0G} represents the second derivative of the electronic and nuclear repulsion energy E evaluated at equilibrium $\mathbf{u} = \mathbf{0}$ with respect to the displacement of atom A in cell 0 ($u_i = x_i - x_i^*$) and displacement of atom B in cell G ($u_j = x_j - x_j^*$) from their equilibrium position x_i^*, x_j^*:

$$\sum_G H_{ij}^{0G} = \sum_G \left[\frac{\partial^2 E}{\partial u_i^0 \partial u_j^G} \right]_0 \quad i=1,\ldots,3N; j=1,\ldots,3N \qquad (3)$$

The calculation of the Hessian at equilibrium is made by the analytical evaluation of the energy first derivatives, Φ_j of E with respect to the atomic displacements:

$$\Phi_j = \sum_G v_j^G = \sum_G \frac{\partial E}{\partial u_j^G} \quad j=1,\ldots,3N \qquad (4)$$

while second derivatives at $\mathbf{u} = \mathbf{0}$ (where all first derivatives are zero) are calculated numerically using a "two-point" formula:

$$\left[\frac{\partial \Phi_j}{\partial u_i^0} \right]_0 \approx \frac{\Phi_j(0,\ldots,u_i^0,\ldots,0) - \Phi_j(0,\ldots,u_i^0,\ldots,0)}{u_i^0}$$
$$i=1,\ldots,3N; j=1,\ldots,3N \qquad (5)$$

More details on the algorithms used by the CRYSTAL code to calculate the vibrational properties of a 3D system can be found in dedicated literature (Pascale et al. 2004; Tosoni et al. 2005). The Hessian matrix eigenvalues provide the normal harmonic frequencies ω_h, and they are obtained with $3N + 1$ SCF and gradient calculation. This method can be quite demanding for large unit cells, but point symmetry facilitates a remarkable time saving, because only the lines of the Hessian matrix referring to irreducible atoms need to be generated.

Results

Geometry optimization

The optimization of the pyrophyllite was made on the primitive cell ($P\bar{1}$) to reduce the computational costs of the procedure, and then, the results were reported in terms of the crystallographic cell. A detailed description of the data obtained by GTO/B3LYP-D* approach is presented in Table 1 alongside XRD structural refinement (Lee and Guggenheim 1981; Wardle and Brindley 1972) and very recent theoretical results (Tunega et al. 2012) reported in literature.

The adoption of the modified Grimme's dispersion parameters (B3LYP-D*) provided lattice parameters and bond lengths in very good agreement with experimental data, with only a small under-estimation of the cell volume (0.4 %). In particular, the description of the **c** axis is adequately accurate. Compared to the plane-waves/PBE-D approach (Tunega et al. 2012), we provide similar results in the description of the lattice axis *a*, *b* and in particular *c*, but there are some differences in the unit-cell angles, especially β. The volume contraction is also very similar.

The internal geometry, namely the mean bond lengths, is very similar to that obtained by previous theoretical study. Both results are slightly larger than experimental values of about 0.7 %. Pyrophyllite, as other phyllosilicates, has a distorted hexagonal tetrahedral sheet due to the non-ideal SiO_4^{4-} tetrahedrons. The same observation can be extended to the octahedral sheet. According to literature (Bailey 1988), the tetrahedral rotation angle is defined as

$$\alpha = 1/2 \left(\sum_{i=1}^6 \phi_i - 120^\circ \middle/ 6 \right) \qquad (6)$$

where ϕ_i is the angle described by triples of basal oxygen atoms. We obtained $\alpha = 23.82°$ in our simulations, a value

Table 1 Theoretical unit-cell constants and experimental lattice parameters and internal geometry of pyrophyllite

Pyrophyllite	Single-crystal XRD		Theoretical	
	(1)	(2)	B3LYP-D* (3)	PBE-D (4)
Lattice				
a (Å)	5.160	5.1614	5.168	5.167
b (Å)	8.966	8.9576	8.956	8.978
c (Å)	9.347	9.3511	9.317	9.300
α (°)	91.18	91.03	90.96	90.97
β (°)	100.46	100.37	101.80	100.91
γ (°)	89.64	89.75	89.97	89.73
Basal *d* spacing (Å)	9.192	9.198	9.120	9.132
V_{cc} (Å³)	425.157	425.206	423.316	423.610
Mean bond lengths (Å)				
Si–O[b]	1.6117	–	1.6236	1.6280
Si–O[a]	1.632	–	1.6461	1.6480
Al–O	1.924	–	1.9290	1.9230
Al–O[h]	1.8885	–	1.8938	1.8940
O–H	–	–	0.9582	0.9710

V_{cc} refers to the crystallographic cell volume

(1) Lee and Guggenheim (1981)

(2) Wardle and Brindley (1972)

(3) This study

(4) Tunega et al. (2012)

in good agreement with the experimental one (20.4°) (Lee and Guggenheim 1981). The octahedral rotation angle is given by

$$\cos \psi = \Phi_0 \big/ 2\langle M - O, \text{OH} \rangle \qquad (7)$$

with Φ_0 the thickness of the O-layer (Å) and $\langle M - O, \text{OH} \rangle$ the mean bond lengths in the octahedrons. The obtained ψ value is 56.0°, in good agreement with the experimental value, $\psi = 57.1°$ (Lee and Guggenheim 1981). According to Lee and Guggenheim (1981), the tetrahedral rotation reduces the lateral dimensions of the tetrahedral sheet. Since tetrahedral faces may be approximately described as equilateral triangles, the resulting distance between apical oxygens, AO_a, may be calculated as

$$AO_a = \left[2e_{\text{th}} \cos \left(\alpha / 2 \right) \right] \big/ \sqrt{3} \qquad (8)$$

where e_{th} is the mean tetrahedral edge length. In the B3LYP-D* simulated structure, the AO_a value is 3.01 Å, in very good agreement with the observed 3.00 Å obtained from XRD refinement (Lee and Guggenheim 1981).

Regarding the hydrogen atom position, the free relaxation of the mineral geometry led the O–H bond direction canted by about 59.87° with respect to the [001] direction, pointing versus the octahedral vacancy (see Fig. 1).

Phonon calculations

The vibrational features of pyrophyllite were simulated in the primitive cell, which has 20 atoms. The number of normal modes is given by $20 \times 3 = 60$, and three of them are related to translation of the whole unit cell. The remnant 57 modes are vibrational and subdivided as:

$$\Gamma_{\text{tot}} = 30A_g + 27A_u$$

Modes with A_g symmetry are Raman-active, while A_u ones are IR-active. None of them exhibits symmetry-related degeneracies, and thus, the IR and Raman spectra have 27 and 30 signals, respectively. We report in Table 2 the results obtained from our simulated IR/Raman analysis and the calculated IR spectrum in Fig. 2. The analysis of the vibrational modes has been conducted with the aid of the visualization software MOLDRAW (Ugliengo et al. 1993) and the potential energy distribution (PED) computed by CRYSTAL09.

The region between 0 and 400 cm^{-1}, which is not completely shown in the spectrum of Fig. 2, is characterized by eight low-intensity phonon modes. The first intense peak is composed by two Al–O^a–Al modes which fall at 474 and 488 cm^{-1}, respectively. From the PED analysis, an OH libration component in the signal at 488 cm^{-1} was found. The peak in the range 500–600 cm^{-1} is formed by three signals at 533, 549 and 556 cm^{-1}, related to Si–O^a–Al

bending modes. Again, the mode at 556 cm^{-1} exhibits an OH libration component. Two modes related to O^a–Si–O^b bending have been identified. The first one is at 643 cm^{-1}, but is not visible in the spectrum because of low intensity. The second is associated with an "umbrella" bending mode at 749 cm^{-1}, faintly visible.

In the spectral region above 800 cm^{-1}, there are the Si–O stretching modes. There are two low-intensity signals at 819 and 842 cm^{-1}, which have been assigned to symmetric Si–O^b stretching vibrations. Two modes have been identified as Si–O^a stretching: one is at 849 cm^{-1}, but it is very faint and overlapped to the one at 842 cm^{-1}; the other is at 908 cm^{-1}, with high intensity. Finally, three signals are related to the asymmetric Si–O^b stretching modes, at 1048 (very intense), 1063 (very intense) and 1107 cm^{-1} at low intensity.

Regarding OH phonon modes, there is a medium-intensity signal at 1016 cm^{-1}, related to a pure OH libration mode, and the OH stretching mode at 3886 cm^{-1}. When anharmonicity was taken into account, the latter fell at 3709 cm^{-1}, with an anharmonic constant of 82 cm^{-1}. Unfortunately, the CRYSTAL09 code does not extend the anharmonic calculation to other modes but the stretching one, preventing the calculation of the anharmonicity of OH libration modes.

The simulated infrared spectrum is in reasonable agreement with the one reported in the experimental works of Mukhopadhyay et al. (2010) and of Ogorodova et al. (2011). The differences are imputable to the considered model, which is an end-member of the pyrophyllite mineral.

Equation of state of pyrophyllite

The P–T behaviour of any solid insulator can be derived from the Helmholtz energy F (Anderson 1995).

$$F = E_{\text{ST}}(V) + F_{\text{VIB}}(V, T) \qquad (9)$$

where E_{ST} is the potential of a static lattice at absolute zero (athermal limit) and F_{VIB} is the vibrational energy related to the thermal motion of the atoms. The pressure can be obtained by the first derivative of Eq. (9).

$$P = -\left(\frac{\partial F}{\partial V} \right)_T = -\left(\frac{\partial E_{\text{ST}}}{\partial V} \right)_{T=0} + \left(\frac{\partial F_{\text{VIB}}}{\partial V} \right)_T \qquad (10)$$

In the present work, the evaluation of the pyrophyllite equation of state is subdivided into two subsections. In the first one, only the static lattice values of the mineral are obtained and an atomic description of the pressure-induced variations to the structure is provided. In the second one, the thermal contribution is included to evaluate the thermomechanical properties of the mineral at different temperatures.

Table 2 Calculated pyrophyllite harmonic phonon frequencies

Mode	IRREP	Active	Frequency (cm^{-1})	IR Intensity	Exp (1)	Exp (2)
O^a–H–O^b	A_u	IR	411	220		
O^a–H–O^b	A_u	IR	424	49		420
O^a–H–O^b	A_u	IR	427	28		
	A_g	R	436	0		
	A_g	R	454	0		
Al–O^a–Al	A_u	IR	474	1318		
	A_g	R	477	0		
Si–O^a–Al + OH libration	A_u	IR	488	1532		
	A_g	R	502	0		
	A_g	R	531	0		
Si–O^a–Al	A_u	IR	533	352		
	A_g	R	546	0		
Si–O^a–Al	A_u	IR	549	640		537
Si–O^a–Al + OH libration	A_u	IR	556	937		579
	A_g	R	613	0		
O^a–Si–O^b bending	A_u	IR	643	2		625
	A_g	R	656	0		
	A_g	R	718	0		
O^a–Si–O^b "umbrella"	A_u	IR	749	49		
	A_g	R	819	0		
Si–O^b symm	A_u	IR	819	165		814
Si–O^b symm	A_u	IR	842	183		835
	A_g	R	849	0		
Si–O^a in phase	A_u	IR	849	13		853
Si–O^a out of phase/Al-(OH)	A_u	IR	908	2399	950	949
	A_g	R	927	0		
OH libration	A_u	IR	1016	616		
	A_g	R	1021	0		
Si–O^b symm	A_u	IR	1048	2570	1046	1048
	A_g	R	1049	0		
Si–O^b symm	A_u	IR	1063	2204		1067
	A_g	R	1065	0		
	A_g	R	1078	0		
Si–O^b symm/Al-(OH)	A_u	IR	1107	244	1120	1119
	A_g	R	1110	0		
	A_g	R	3884	0		
OH stretching (harmonic)	A_u	IR	3886	551		
OH stretching (anharmonic)	A_u	IR	3709	–		3669

(1) Mukhopadhyay et al. (2010)

(2) Ogorodova et al. (2011)

Static calculations

The description of the compressional behaviour of a solid phase within the periodic boundary conditions has been conducted with the EOS algorithm present in the CRYSTAL09 code (Ottonello et al. 2009a). With this method, starting from the optimized pyrophyllite structure, a cell optimization is carried out with a symmetry-preserving relaxation procedure by exploring, at selected volumes, the minimum energy *a/b* and *c/b* ratios and internal coordinates. We considered twenty volumes between $0.90V_{init}$ and $1.10V_{init}$, where V_{init} is the volume of the original unit cell. The relaxed lattice parameters at the athermal limit are reported in Table 3. The partial derivation of a third-order polynomial fit on the computed $E(V)$ curve (Fig. 3a) reproduced the local values of the ab initio pressure, allowing

the analysis of the functional dependence of the structural details on P at $T = 0$:

$$P_{st} = -\left(\frac{\partial E}{\partial V}\right)_{T=0} = 3p_1 V^2 + 2p_2 V + p_3 \quad (11)$$

with $p_1 = -5.27514 \times 10^{-7}$, $p_2 = 3.63107 \times 10^{-4}$ and $p_3 = -0.0828$ the fitting parameters ($R = 0.99994$). A graphical representation of $V(P_{st})$ trend is shown in Fig. 3b.
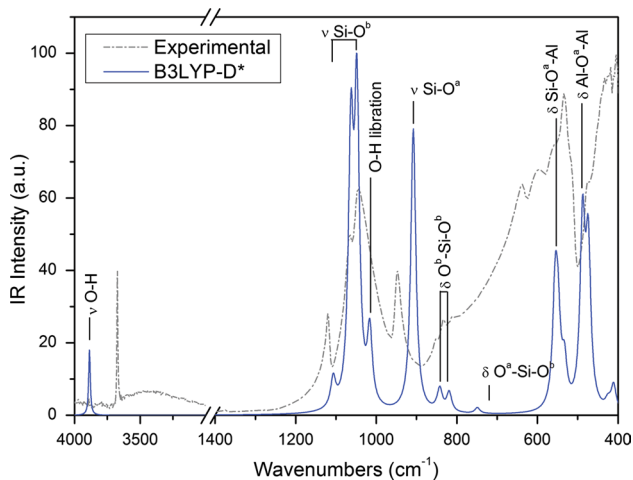
Fig. 2 Simulated infrared spectrum of pyrophyllite. The experimental IR spectrum is from the work of Mukhopadhyay et al. (2010)

Pyrophyllite volume versus P_{st} data were fitted using a third-order finite strain isothermal Birch–Murnaghan equation of state (III-BM EOS) (Birch 1947):

$$P_{III-BM} = \frac{3}{2} K_{T0} \left[\eta^{-7/3} - \eta^{-5/3}\right]$$
$$\times \left\{1 - \frac{3}{4}(4 - K')\left(\eta^{-2/3} - 1\right)\right\} + P_0 \quad (12)$$

where $\eta = V/V_0$ is a dimensionless parameter and V_0 is the volume at reference pressure P_0. The best fitting procedure was made by least-square method, using the EOS-FIT5.2 software (Angel 2001). We obtained the refined elastic parameters at $T = 0$ K: $V_0 = 423.26(20)$ Å³, $K_{T0} = 48.63(69)$ GPa and $K' = 11.14(43)$.

In Fig. 4a, b, we report the evolution of axial and angular lattice parameters at different pressures, respectively. Regarding the compressive regime ($P > 0$ GPa), the calculated trend is monotonic. It is graphically clear that pyrophyllite deformation exhibits a strongly anisotropic behaviour, with smaller variations for a and b cell parameters than for the c one. It is possible to describe the observed anisotropy calculating the axial bulk moduli with a III-BM EOS fit on the lattice parameters values at different pressures. The obtained refined data for the a axis, b axis and c axis were, respectively: $a_0 = 5.181(1)$ Å, $K_{T0}(a) = 83.63(55)$ GPa and $K'(a) = 3.25(41)$; $b_0 = 8.977(1)$ Å, $K_{T0}(b) = 101.94(93)$ GPa and

Table 3 Simulated unit-cell constants of pyrophyllite at different volumes

Volume (Å³)	a (Å)	b (Å)	c (Å)	α (°)	β (°)	γ (°)	P_{st} (GPa)	V/V_0
380.520	5.040	8.736	8.825	90.149	101.619	90.236	8.3590	0.8990
384.798	5.055	8.765	8.867	90.215	101.603	90.216	7.2332	0.9091
389.099	5.070	8.794	8.910	90.286	101.585	90.194	6.1658	0.9193
393.413	5.084	8.822	8.954	90.359	101.568	90.170	5.1589	0.9295
397.760	5.098	8.849	9.001	90.435	101.553	90.144	4.2094	0.9397
402.092	5.111	8.875	9.048	90.511	101.548	90.117	3.3286	0.9500
406.451	5.124	8.900	9.098	90.587	101.555	90.088	2.5081	0.9603
410.834	5.136	8.923	9.151	90.669	101.580	90.057	1.7477	0.9706
415.242	5.148	8.945	9.207	90.755	101.626	90.025	1.0501	0.9811
419.669	5.160	8.966	9.266	90.840	101.697	89.994	0.4170	0.9915
423.316	*5.168*	*8.956*	*9.317*	*90.960*	*101.800*	*89.970*	*−0.0530*	*1.0001*
424.098	5.170	8.985	9.328	90.922	101.782	89.962	−0.1479	1.0020
428.612	5.180	9.002	9.393	90.996	101.862	89.931	−0.6547	1.0126
433.109	5.189	9.018	9.462	91.060	101.940	89.902	−1.0898	1.0233
437.631	5.197	9.031	9.535	91.081	102.001	89.875	−1.4563	1.0339
442.159	5.203	9.041	9.614	91.085	101.060	89.854	−1.7531	1.0446
446.703	5.207	9.048	9.701	91.057	102.155	89.839	−1.9796	1.0554
451.242	5.209	9.051	9.800	90.983	102.348	89.829	−2.1351	1.0661
455.855	5.209	9.050	9.918	90.856	102.812	89.826	−2.2201	1.0770
460.491	5.206	9.044	10.092	90.466	104.276	89.834	−2.2315	1.0879
465.106	5.205	9.041	10.215	90.259	104.618	89.839	−2.1693	1.0989

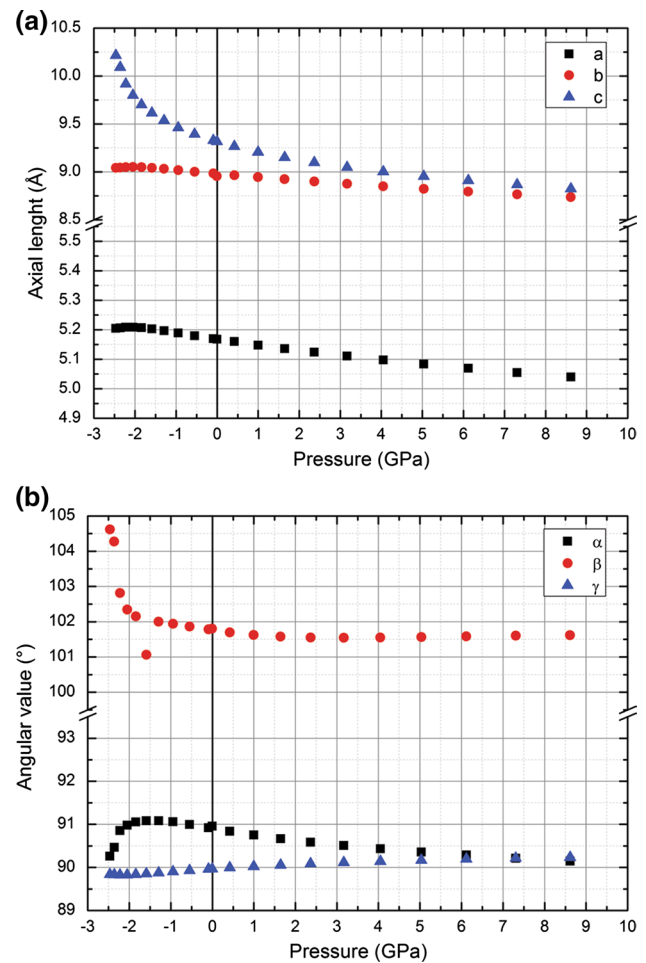Values in italic are related to the pyrophyllite equilibrium geometry

(a)

(b)
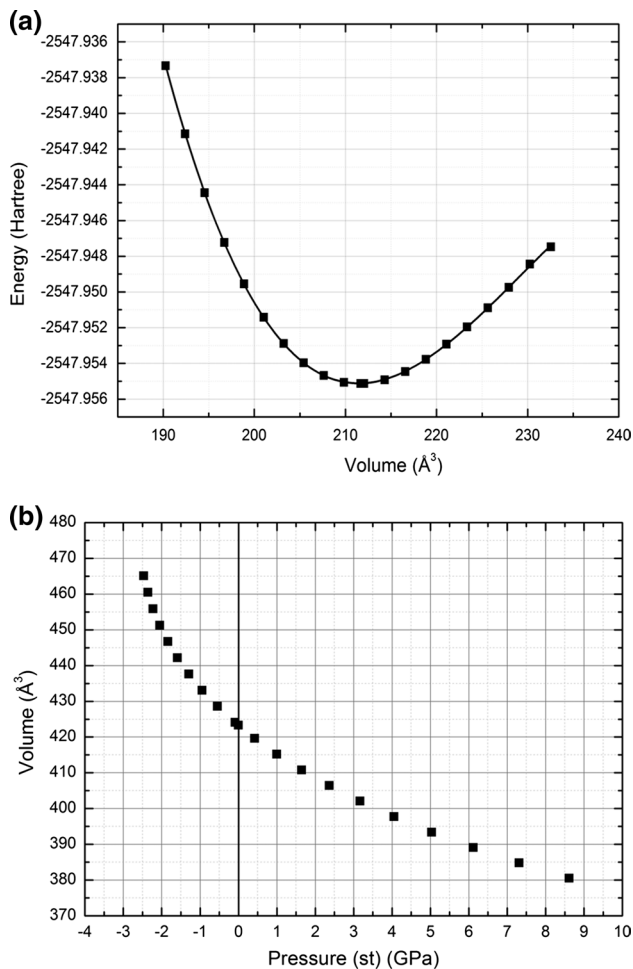
Fig. 3 Calculated energy/volume (**a**) and related volume/pressure (**b**) diagrams for the pyrophyllite unit cell

(a)

(b)

Fig. 4 Compressional behaviour of pyrophyllite (**a**) axial and (**b**) angular parameters under compression and expansion

$K'(b) = 3.17(28)$; $c_0 = 9.311(1)$ Å, $K_{T0}(c) = 27.74(10)$ GPa and $K'(c) = 8.16(3)$. The axial compressibilities, described as $\beta = 1/3K_{T0}$, are in ratio $\beta(a):\beta(b):\beta(c) = 1.219:1.000:3.674$. The obtained axial values are very close to those reported in a previous work on talc (Ulian et al. 2014). This is not surprising because the covalent bonds in the dioctahedral TOT layers are less compressible than the interlayer dominated by Columbian and van der Waals forces (*c* direction).

Regarding the unit-cell angles, we observed a constant decrease of the α parameter and an increase of the γ one in the investigated pressure range. However, the β angle value decreased from 0 to 3.3 GPa and then increased up to 8 GPa.

Based on the unit-cell axial and angular values, we predict a spinodal instability in pyrophyllite upon expansion by about 4.5 % from the zero-pressure volume. According to the literature (Stixrude 2002), the spinodal consists in that point where the bulk modulus vanishes, i.e. where

pressure is extremal, reaching a minimum value beyond which it decreases no more upon further expansion. At the spinodal, pyrophyllite is mechanically unstable and would be expected to fragment. Our results suggest that the spinodal coincides with the hydrostatic tensile strength of −1.6 GPa, in a defect-free, single crystal of pyrophyllite. This value is very similar to that of talc, found by the DFT simulations of Stixrude (2002). It is worth noting that this quantity is different from the usual tensile strength which is measured under uniaxial tension in minerals and materials in generals. It is expected that the uniaxial tensile strength may be less than the value calculated for hydrostatic tensile strength, because pyrophyllite is a slightly anisotropic mineral.

In the explored volume range, we observed a strong variation of the interlayer thickness (−13 % at 8 GPa), but the TOT thickness is almost unaffected (−2 % at 8 GPa). The ⟨Si–O⟩ and ⟨Al–O⟩ bond lengths span from 1.631 and 1.926 Å (lower limit) to 1.620 and 1.886 Å (upper limit), respectively. More in detail, in the SiO$_4$ tetrahedrons the

Si–O^a distances are slightly more influenced than the Si–O^b ones, but in AlO$_6$ octahedrons we did not find the same trend.

Furthermore, we noticed that the expansion of the unit cell causes an increase in the distortion index both tetrahedrons and octahedrons, while the compression leads to the opposite behaviour. Similarly to talc structure (Ulian et al. 2014), the increase in pressure is followed by higher rotation angle α (34.88° at 10 GPa) than that of the uncompressed pyrophyllite structure. Expanding the unit cell, α diminishes to 20.06° at −2 GPa.

Negligible O–H bond length and Al–O–H angle variations in the pressure range investigated have been observed.

Thermal contribution and thermomechanical properties

In statistical thermodynamics, the vibrational energy is given by

$$F_{VIB} = -kT \ln Z \tag{13}$$

with Z the partition function calculated by taking the sum of all quantum energy levels for each independent oscillators in the solid lattice and given by:

$$Z = \sum_i e^{-\varepsilon_i/kT} \tag{14}$$

The ε_i values are the eigenvalues of the energy operator, which can be used to define the partition function, Z_i, for each vibrational mode, ϖ_i,

$$\varepsilon_i = \frac{1}{2}\hbar\varpi_i, \frac{3}{2}\hbar\varpi_i, \frac{5}{2}\hbar\varpi_i, \text{etc}\dots \tag{15}$$

$$Z_i = e^{-\hbar\varpi_i/2kT} \sum_{i=0}^{\infty} e^{-3\hbar\varpi_i/2kT} = \frac{e^{-\hbar\varpi_i/2kT}}{\left(1 - e^{-\hbar\varpi_i/kT}\right)} \tag{16}$$

Table 4 Pyrophyllite vibrational frequencies at 0 GPa and related mode gamma

N	ν (cm^{-1})	Mode	IR, Raman	γ_i	N	ν (cm^{-1})	Mode	IR, Raman	γ_i
1	111.3	Acoustic	A, I	–	30	476.9	A_g	I, A	0.2
2	111.3	Acoustic	A, I	–	31	487.6	A_u	A, I	0.2
3	186.5	Acoustic	A, I	–	32	501.8	A_g	I, A	0.2
4	105.4	A_g	I, A	1.2	33	531.2	A_g	I, A	0.5
5	118.1	A_g	I, A	1.2	34	532.9	A_u	A, I	0.5
6	152.3	A_u	A, I	−0.1	35	545.5	A_g	I, A	0.4
7	188.2	A_g	I, A	0.9	36	549.0	A_u	A, I	0.4
8	188.3	A_u	A, I	0.3	37	555.6	A_u	A, I	0.3
9	189.2	A_u	A, I	0.3	38	613.4	A_g	I, A	0.4
10	208.8	A_u	A, I	1.0	39	642.5	A_u	A, I	0.3
11	209.4	A_g	I, A	1.3	40	656.1	A_g	I, A	0.2
12	219.2	A_g	I, A	1.3	41	717.7	A_g	I, A	0.3
13	263.5	A_u	A, I	0.5	42	749.1	A_u	A, I	0.2
14	267.3	A_g	I, A	0.7	43	818.8	A_g	I, A	0.2
15	301.9	A_g	I, A	0.2	44	818.9	A_u	A, I	0.2
16	320.8	A_g	I, A	0.1	45	841.9	A_u	A, I	0.2
17	340.6	A_u	A, I	0.2	46	848.9	A_g	I, A	0.3
18	345.4	A_g	I, A	0.3	47	849.0	A_u	A, I	0.3
19	346.2	A_u	A, I	0.5	48	907.5	A_u	A, I	0.2
20	362.7	A_u	A, I	0.1	49	926.7	A_g	I, A	0.3
21	380.4	A_g	I, A	0.2	50	1015.5	A_u	A, I	0.2
22	384.0	A_g	I, A	0.3	51	1021.0	A_g	I, A	0.2
23	398.5	A_g	I, A	0.4	52	1048.5	A_u	A, I	0.1
24	410.8	A_u	A, I	0.1	53	1049.3	A_g	I, A	0.1
25	424.0	A_u	A, I	0.2	54	1063.3	A_u	A, I	0.1
26	426.9	A_u	A, I	0.4	55	1065.1	A_g	I, A	0.1
27	436.4	A_g	I, A	0.2	56	1078.0	A_g	I, A	0.2
28	453.8	A_g	I, A	0.3	57	1107.2	A_u	A, I	0.0
29	473.5	A_u	A, I	0.2	58	1110.3	A_g	I, A	0.0
30	476.9	A_g	I, A	0.2	59	3883.9	A_g	I, A	0.0
31	487.6	A_u	A, I	0.2	60	3886.5	A_u	A, I	0.0

It is then possible to define the contribution to the Helmholtz free energy from each vibrational mode as:

$$F_{\mathrm{VIB}_i} = -kT \ln Z_i = \frac{\hbar \varpi_i}{2kT} \ln \left(1 - e^{\hbar \varpi_i / kT} \right) \quad (17)$$

which can then be summed over the $3n - 3$ oscillators (n the number of atoms in the unit cell) in the considered lattice to obtain the whole thermal contribution to the free energy

$$F_{\mathrm{VIB}} = \frac{1}{2} \sum_{i=1}^{3n-3} \hbar \varpi_i + kT \sum_{i=1}^{3n-3} \ln \left(1 - e^{-\hbar \varpi_i / kT} \right) \quad (18)$$

The first addendum of Eq. (18) represents the zero-point energy (E_{ZP}) of the solid, unaffected by the temperature, and the second term is the energy arising from excitation due to temperature (F_{TH}). The term $\hbar \varpi_i / kT$ can be substituted with X_i to simplify the expression

$$F_{\mathrm{VIB}} = \frac{kT}{2} \sum_{i=1}^{3n-3} X_i + kT \sum_{i=1}^{3n-3} \ln \left(1 - e^{-X_i} \right) \quad (19)$$

Applying Eq. (19) to Eq. (10) allows finding the pressure related to each volume transformation

$$P = -\left(\frac{\partial E_{\mathrm{ST}}}{\partial V} \right)_{T=0} + \frac{kT}{2V} \sum_{i=1}^{3n-3} \gamma_i X_i + \frac{kT}{V} \sum_{i=1}^{3n-3} \gamma_i \frac{X_i}{e^{X_i} - 1} \quad (20)$$

where γ_i is the Grüneisen's mode gamma of each vibrational frequency, given by

$$\gamma_i = \frac{\partial \ln \varpi_i}{\partial \ln V} \quad (21)$$

The mode gammas for pyrophyllite are summarized in Table 4.

In the quasiharmonic treatment, the vibrational modes are dependent only on volume variations. The thermodynamic properties are dependent on temperature by the second term of Eq. (18) (Anderson 1995; Ottonello et al. 2009a, b). Rewriting Eq. (20) in terms of pressure P, we can obtain:

$$P = P_{\mathrm{ST}} + P_{\mathrm{ZP}} + P_{\mathrm{TH}} = P_{\mathrm{T=0}} + P_{\mathrm{TH}} \quad (22)$$

where the static pressure (P_{ST}) is corrected by the zero-point energy (P_{ZP}) and by the thermal contribution (P_{TH}). $P_{\mathrm{T=0}}$, the thermal pressure, is equal to $P_{\mathrm{ST}} + P_{\mathrm{ZP}}$.

The above formulations were enriched by the calculation of pyrophyllite phonon dispersion for each simulated volume. Dispersion effects were simulated from vibrational frequencies in the case of super-cells (we adopted a $2 \times 2 \times 2$ one), which allows considering eight k points. The obtained results are very close to those calculated

without considering the phonon dispersion effects (ca. 1.4 kJ/mol). Then, the related thermodynamic quantities (pressure, bulk moduli, etc.) are almost unaffected by phonon dispersion. This is in good agreement with previous observations, which stated that the Grüneisen's parameters corresponding to the vibrational modes calculated in the Γ point only are reasonably representative of the whole set of parameters, because they are numerous and depend upon the number of atoms in the unit cell. Indeed, other authors (Ottonello et al. 2009a, b; Prencipe et al. 2011; Ulian and
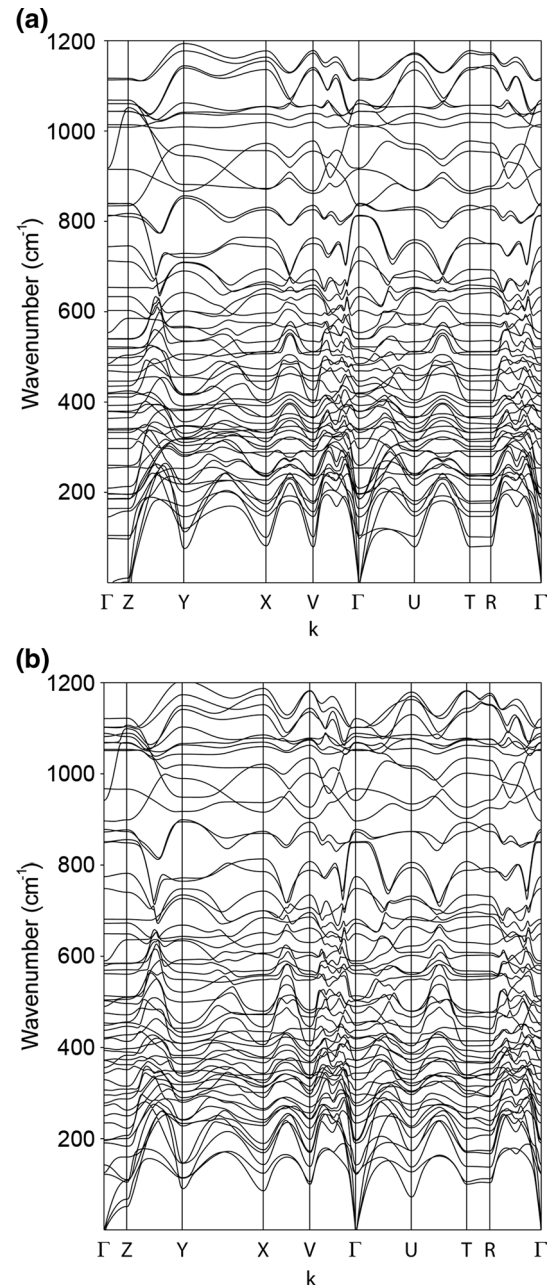
Fig. 5 Pyrophyllite phonon dispersion calculated at **a** −2.2 GPa and **b** 8.4 GPa

Table 5 Volume (Å³) values at different temperatures and pressures for pyrophyllite and fit parameters of the third-order Birch–Murnaghan EoS
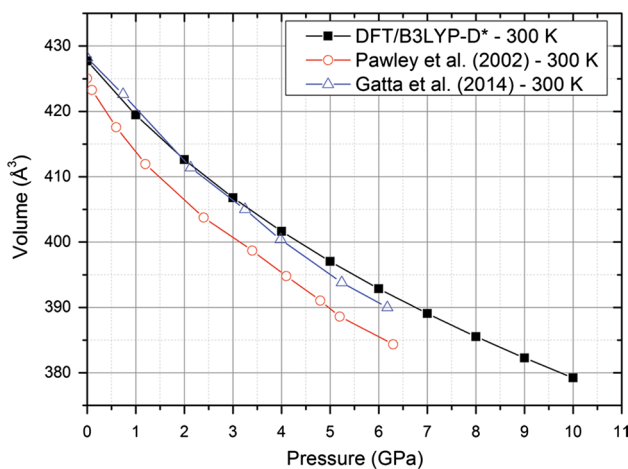
T (K)	Pressure (GPa)											V_0 (Å³)	K_T (GPa)	$K_T{}'$
	0	1	2	3	4	5	6	7	8	9	10			
0	423.264	415.217	408.603	402.947	397.985	393.552	389.537	385.864	382.474	379.325	376.383	423.26(20)	48.63(69)	11.14(43)
10	426.423	418.342	411.646	405.894	400.832	396.300	392.191	388.427	384.952	381.721	378.701	426.42(20)	47.33(70)	10.54(43)
50	426.435	418.351	411.653	405.899	400.836	396.304	392.194	388.429	384.954	381.723	378.702	426.44(20)	47.30(70)	10.54(43)
100	426.540	418.433	411.721	405.956	400.884	396.345	392.230	388.461	384.982	381.747	378.724	426.54(20)	47.17(70)	10.55(43)
150	426.743	418.602	411.866	406.084	400.998	396.448	392.323	388.546	385.059	381.818	378.789	426.74(20)	46.97(70)	10.56(43)
200	427.018	418.839	412.076	406.272	401.170	396.605	392.468	388.680	385.183	381.934	378.898	427.02(20)	46.77(70)	10.55(43)
250	427.346	419.128	412.336	406.509	401.387	396.806	392.655	388.855	385.347	382.088	379.043	427.34(20)	46.56(71)	10.54(44)
300	427.714	419.457	412.635	406.783	401.641	397.043	392.876	389.062	385.543	382.272	379.217	427.72(20)	46.37(71)	10.51(44)
350	428.112	419.816	412.963	407.087	401.924	397.307	393.124	389.296	385.763	382.481	379.415	428.12(20)	46.19(72)	10.48(44)
400	428.532	420.198	413.315	407.413	402.228	397.592	393.393	389.550	386.003	382.709	379.631	428.54(20)	46.03(73)	10.45(44)
450	428.968	420.598	413.685	407.758	402.551	397.895	393.679	389.820	386.260	382.952	379.863	428.96(20)	45.87(74)	10.41(45)
500	429.416	421.011	414.068	408.116	402.887	398.212	393.978	390.103	386.528	383.208	380.106	429.42(20)	45.73(75)	10.36(45)
600	430.337	421.865	414.865	408.862	403.589	398.875	394.606	390.699	387.095	383.747	380.621	430.34(20)	45.48(76)	10.26(45)
700	431.275	422.743	415.688	409.637	404.321	399.567	395.262	391.323	387.689	384.315	381.163	431.28(20)	45.28(79)	10.15(45)
800	432.220	423.633	416.527	410.430	405.071	400.279	395.939	391.968	388.304	384.902	381.724	432.22(20)	45.12(81)	10.04(45)
900	433.163	424.529	417.376	411.234	405.834	401.005	396.630	392.626	388.933	385.503	382.299	433.16(19)	45.01(83)	9.91(45)

Valdrè 2014a, b) demonstrated that it is possible to obtain reliable estimations of thermoelastic and thermodynamics quantities by neglecting dispersion effects, even with systems having relatively small unit cells. It is also worth noting that, according to the study of Kieffer (1979a), mineral thermodynamic properties, calculated as averages over the relevant quantities at the atomic level, can be obtained with high reliability even without a detailed knowledge of the phonon density of state. For completeness, we included phonon dispersion spectra at -2.2 GPa and at 8.4 GPa (athermal conditions), to show how small is the pressure influence on the pyrophyllite phonon behaviour (see Fig. 5).

In Table 5, the corrected pressure values for Eq. (20) are reported for the range of temperatures from 0 to 900 K.
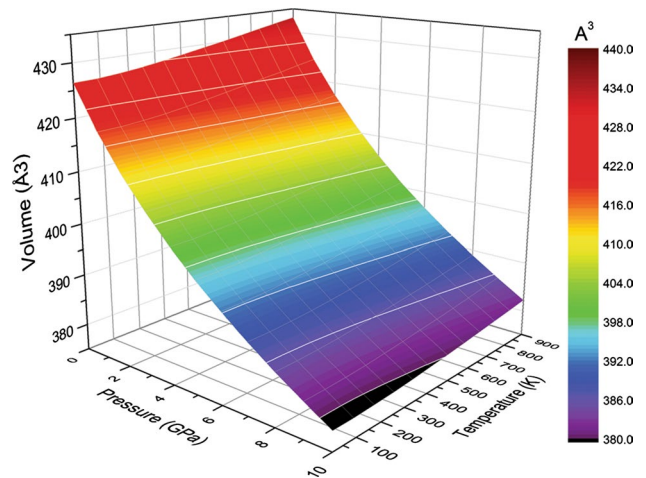
The thermal bulk modulus (K_T) at a given cell volume (pressure) and temperature has been calculated by the third-order BM3 EOS. Using isothermal curves, at different T, we can obtain at each temperature the bulk modulus (K_T), its first derivative (K') and reference volume (V_0), at any fixed reference pressure. The calculated $V(P, T)$ values for $T = 300$ K are in good agreement with those experimentally obtained by Pawley et al. (2002) on a powdered pyrophyllite sample, and even better comparison can be made on those reported very recently by Gatta et al. (2014) (Fig. 6). In Fig. 7, we report the $V(P, T)$ of pyrophyllite calculated in the ranges 0–10 GPa and 0–900 K.

Regarding the axial compressibility at room temperature, we fitted by the third-order Birch–Murnaghan equation the a axis, b axis and c axis data, obtaining, respectively: $a_0 = 5.189(1)$ Å, $K_{T0}(a) = 89.46(75)$ GPa and $K'(a) = 3.00(1)$; $b_0 = 8.990(7)$ Å, K_{T0} $(b) = 109.01(1.37)$ GPa and $K'(b) = 3.00(1)$; $c_0 = 9.368(1)$ Å, $K_{T0}(c) = 26.03(8)$ GPa and $K'(c) = 8.12(3)$.

The related axial compressibilities are $\beta(a) = 3.73 \times 10^{-3}$, $\beta(b) = 3.06 \times 10^{-3}$ and $\beta(c) = 12.8 \times 10^{-3}$ GPa^{-1}, in ratio $\beta(a):\beta(b):\beta(c) = 1.218:1.000:4.188$.

Fig. 7 Compressional behaviour of pyrophyllite between 0 and 10 GPa and 10–900 K
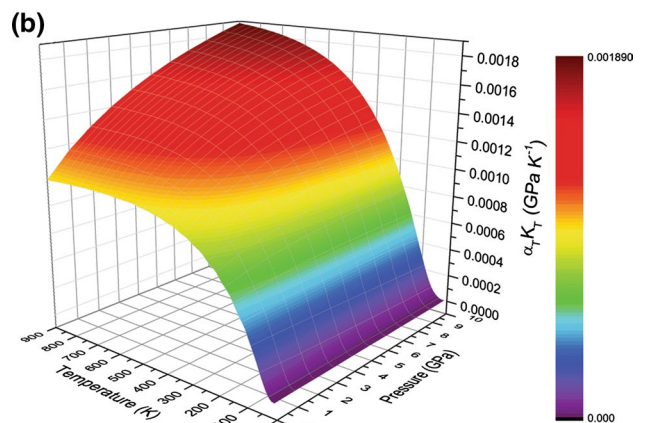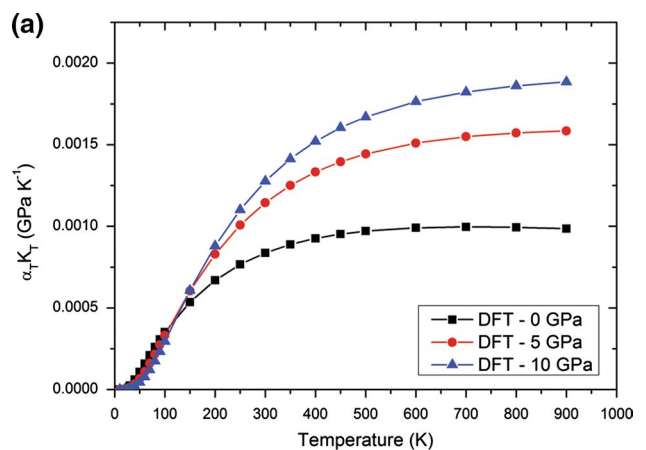

Fig. 6 Comparison between theoretical pyrophyllite compression at $T = 300$ K (*black line*) and experimental results of Pawley et al. (2002), *red line*, and of Gatta et al. (2014), *blue line*, obtained at the same temperature

Fig. 8 a Isobaric $\alpha_T K_T$ product at three different pressures and **b** three-dimensional plot of the $\alpha_T K_T$ product at different pressures and in the temperature range 10–900 K

From the quasi-harmonic mode gamma analysis of the $3n - 3$ optic modes, we obtained the $\alpha_T K_T$ product, by using the formula (Anderson 1995; Ottonello et al. 2010)

$$\alpha_T K_T = \frac{R}{ZV} \sum_{i=4}^{3n} \gamma_i e^{X_i} \left(\frac{X_i}{e^{X_i} - 1} \right)^2 \tag{23}$$

As shown in Fig. 7a, this product asymptotically attains a constant value at high temperatures, depending on the considered pressure. For example, at 0 GPa $\alpha_T K_T$ reaches a constant value of 1.2×10^{-3} GPa/K above the Debye temperature of the mineral (computed $\Theta = 927.17$ K at 0 GPa) (Fig. 8a, b).

We calculated the isobaric temperature derivative of bulk modulus for pyrophyllite by linear regression of the K_T data as a function of temperature in the 100–900 K range. We reported the results in Table 6. It can be observed that the $(\partial K_T / \partial T)_P$ values decrease by increasing the pressure, with a ratio $(\partial K_T / \partial T \partial P) = -4.95$. It is worth noting that the quasi-harmonic treatment does not consider the fact that K_T would not vary linearly with T.

With the knowledge of the bulk moduli at each P–T condition, obtained from the BM3 EOS fitting, we can directly calculate the thermal expansion coefficient (α_T) of pyrophyllite. We calculated α_T in the P range 0–10 GPa from 10 to 900 K, and the results are reported in Table 7. As it can be observed from the plot in Fig. 9a, the thermal expansion coefficient increases with T, but it is reduced by augmenting the pressure. A complete $\alpha_T(P, T)$ plot is reported in Fig. 9b.

The calculation of thermodynamic properties relies on the Einstein model for optic modes. Within the harmonic approximation, the isochoric heat capacity of a solid insulator can be expressed as (Anderson 1995)

$$C_V = \frac{3R}{Z} \left(\frac{2}{\pi} \right)^3 \sum_{i=1}^{3} \int_0^{X_i} \frac{\left[\arcsin \left(X / X_i \right) \right]^2 X^2 e^X \, dX}{\left(X_i^2 - X^2 \right)^{1/2} \left(e^X - 1 \right)^2} + \frac{R}{Z} \sum_{i=4}^{3n} e^{X_i} \left(\frac{X_i}{e^{X_i} - 1} \right)^2 \tag{24}$$

The first term of Eq. (24) is the acoustic modes contribution described by Kieffer's approach (Kieffer 1979a, b, c), while the second one is related to the optical modes.

Table 6 Pyrophyllite bulk modulus K_T (GPa) at different PT conditions

T (K)	Pressure (GPa)										
	0	1	2	3	4	5	6	7	8	9	10
0	48.6	57.5	67.2	76.4	85.1	93.5	101.6	109.5	117.2	124.7	132.1
10	47.3	57.4	66.7	75.5	83.9	92.0	99.9	107.6	115.0	122.3	129.5
20	47.3	57.4	66.7	75.5	83.9	92.0	99.9	107.6	115.0	122.3	129.5
30	47.3	57.4	66.7	75.5	83.9	92.0	99.9	107.6	115.0	122.3	129.5
40	47.3	57.4	66.7	75.5	83.9	92.0	99.9	107.5	115.0	122.3	129.5
50	47.3	57.4	66.7	75.5	83.9	92.0	99.9	107.5	115.0	122.3	129.5
60	47.3	57.3	66.7	75.5	83.9	92.0	99.9	107.5	115.0	122.3	129.5
70	47.3	57.3	66.7	75.5	83.9	92.0	99.9	107.5	115.0	122.3	129.5
80	47.2	57.3	66.6	75.4	83.9	92.0	99.8	107.5	115.0	122.3	129.4
90	47.2	57.3	66.6	75.4	83.8	91.9	99.8	107.5	114.9	122.2	129.4
100	47.2	57.2	66.6	75.4	83.8	91.9	99.8	107.4	114.9	122.2	129.4
150	47.0	57.0	66.4	75.2	83.6	91.7	99.6	107.2	114.7	122.0	129.2
200	46.8	56.8	66.2	75.0	83.4	91.5	99.3	107.0	114.4	121.7	128.9
250	46.6	56.6	65.9	74.7	83.1	91.2	99.0	106.7	114.1	121.4	128.6
300	46.4	56.4	65.7	74.5	82.8	90.9	98.7	106.4	113.8	121.1	128.2
350	46.2	56.2	65.5	74.2	82.6	90.6	98.4	106.0	113.4	120.7	127.8
400	46.0	56.0	65.2	74.0	82.3	90.3	98.1	105.7	113.1	120.3	127.4
450	45.9	55.8	65.0	73.7	82.0	90.0	97.8	105.3	112.7	119.9	127.0
500	45.7	55.6	64.8	73.4	81.7	89.7	97.4	105.0	112.3	119.5	126.6
600	45.5	55.3	64.4	73.0	81.2	89.1	96.8	104.3	111.6	118.7	125.8
700	45.3	55.0	64.0	72.5	80.7	88.5	96.2	103.6	110.8	118.0	124.9
800	45.1	54.7	63.6	72.1	80.2	88.0	95.5	102.9	110.1	117.2	124.1
900	45.0	54.5	63.3	71.7	79.7	87.4	94.9	102.3	109.4	116.4	123.3
$(\partial K_T/\partial T)_P$	−32.3	−35.1	−41.6	−47.3	−52.6	−57.5	−62.1	−66.4	−70.5	−74.4	−78.2

$(\partial K_T/\partial T)_P$ values are reported in bar K^{-1}

The specific heat at constant pressure (C_P) can be obtained from the relationship

$$C_P = C_V + T\alpha_T^2 K_{T,P} V_{P,T} \qquad (25)$$

where $V_{P,T}$ is the cell volume at pressure P and temperature T, respectively.

The complete calculation of the maximum frequency of each acoustic branch requires the knowledge of the averaged shear and longitudinal wave velocities at each volume (pressure), and these quantities can be obtained by the elastic constants at each compressional state (Perger et al. 2009; Ulian et al. 2014). Due to computational costs, we considered the acoustic mode contribution to the thermochemical properties only at 0 GPa. However, as shown in our previous work on talc (Ulian and Valdrè 2014b), the acoustic contribution to the whole property is very low (<5 %) at room temperature and above. Then, the optical part of Eq. (24) represents an adequate approximation of the heat capacity for $T > 300$ K.

The C_V and C_P values obtained at 0 GPa are plotted in Fig. 10a, alongside previous experimental isobaric heat capacity data of pyrophyllite (Krupka et al. 1979; Robie et al. 1976). There is a very good agreement between theoretical and experimental results above 400 K, but the theoretical results are slightly underestimated in the range between 10 and 400 K. The isobaric heat capacity

calculated with Eq. 26 has been fitted in the range 300–900 K by the Haas–Fisher polynomial expression (Haas and Fisher 1976)

$$C_P = a + bT + cT^{-2} + dT^2 + eT^{-1/2} \qquad (26)$$

with regression coefficients $a = 7.2864 \times 10^2$, $b = 2.9561 \times 10^{-2}$, $c = -3.5316 \times 10^{-5}$, $d = -4.5722 \times 10^{-5}$ and $e = -7.7738 \times 10^3$. The polynomial regression in the chosen temperature range is very accurate, with a mean error of 0.1 J/(mol K). We reported also a three-dimensional plot of the C_P data from 0 to 10 GPa (Fig. 10b) to show how the pressure affects this thermochemical property. It can be observed that, for $T < 500$ K, the isobaric heat capacity decreases upon increasing the pressure, while for $T > 500$ K C_P increases.

Discussion and conclusions

The DFT/B3LYP-D* together with an all-electron GTO basis set proposed in this study proved to be adequately accurate in the description of the pyrophyllite mineral. We have shown in previous works that it is also a good modelling approach for talc and for layered silicates in general (Ulian et al. 2013, 2014; Ulian and Valdrè 2014b). The correct evaluation of the weak interaction forces is crucial for

Table 7 Thermal expansion coefficient (α_T, 10^{-5} K^{-1}) in the pressure range 0–10 GPa at different temperatures

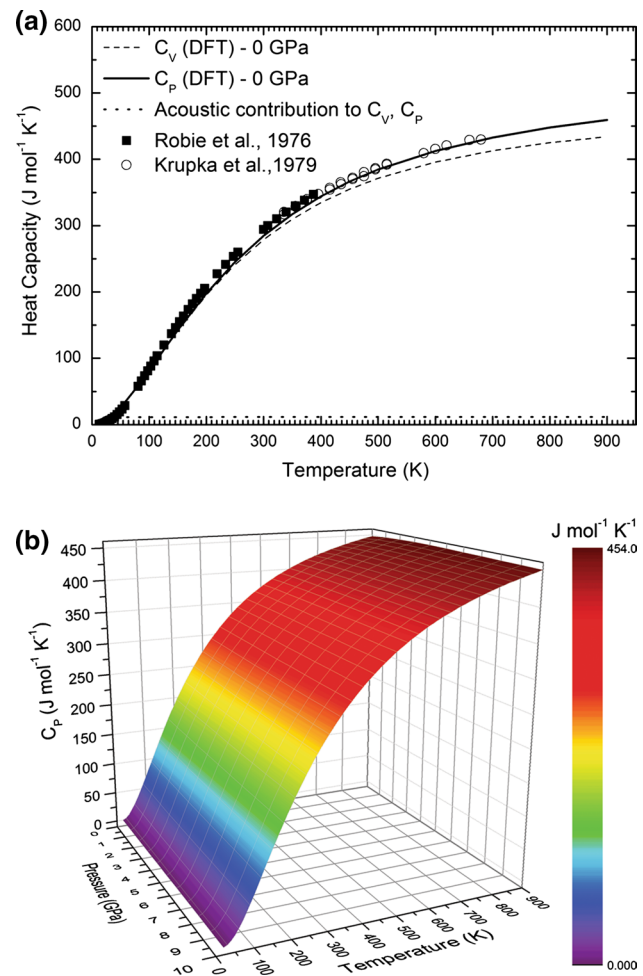| T (K)	Pressure (GPa)										
	0	1	2	3	4	5	6	7	8	9	10
20	0.008	0.005	0.004	0.003	0.002	0.002	0.002	0.001	0.001	0.001	0.001
30	0.052	0.037	0.028	0.021	0.017	0.014	0.012	0.010	0.009	0.007	0.007
40	0.130	0.094	0.072	0.057	0.046	0.038	0.031	0.027	0.023	0.020	0.017
50	0.228	0.170	0.133	0.107	0.088	0.073	0.062	0.053	0.045	0.039	0.034
60	0.336	0.257	0.205	0.168	0.141	0.120	0.103	0.089	0.078	0.068	0.060
70	0.445	0.348	0.284	0.237	0.202	0.175	0.152	0.134	0.118	0.105	0.094
80	0.551	0.440	0.365	0.310	0.268	0.235	0.208	0.185	0.166	0.149	0.135
90	0.652	0.529	0.445	0.383	0.336	0.297	0.266	0.239	0.217	0.197	0.180
100	0.747	0.614	0.523	0.456	0.403	0.360	0.325	0.295	0.270	0.247	0.228
150	1.141	0.984	0.872	0.786	0.716	0.659	0.610	0.568	0.532	0.499	0.470
200	1.431	1.268	1.147	1.051	0.973	0.907	0.850	0.801	0.757	0.718	0.683
250	1.646	1.483	1.359	1.259	1.176	1.104	1.043	0.988	0.940	0.896	0.857
300	1.806	1.647	1.523	1.420	1.334	1.259	1.194	1.137	1.085	1.038	0.996
350	1.924	1.771	1.648	1.545	1.457	1.381	1.313	1.253	1.200	1.151	1.106
400	2.012	1.866	1.744	1.642	1.553	1.476	1.407	1.346	1.290	1.240	1.194
450	2.076	1.937	1.818	1.717	1.628	1.550	1.481	1.419	1.362	1.311	1.263
500	2.123	1.991	1.876	1.775	1.688	1.610	1.540	1.477	1.420	1.367	1.319
600	2.179	2.061	1.954	1.858	1.772	1.695	1.625	1.562	1.504	1.451	1.402
700	2.201	2.099	2.000	1.909	1.826	1.750	1.682	1.619	1.561	1.508	1.459
800	2.203	2.117	2.026	1.940	1.861	1.787	1.720	1.658	1.601	1.548	1.499
900	2.191	2.120	2.039	1.959	1.883	1.812	1.747	1.686	1.630	1.578	1.529

(a)

(b)
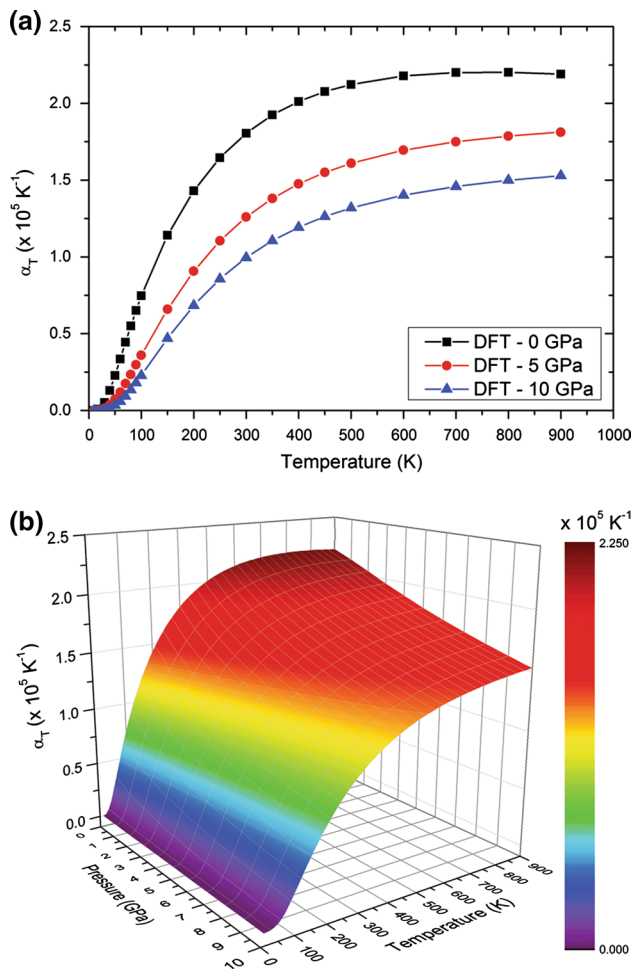
Fig. 9 a Isobaric thermal expansivity (α_T) at three different pressures and **b** three-dimensional plot of the α_T at different pressures and in the temperature range 10–900 K

(a)

(b)

Fig. 10 a Isochoric (*dashed line*) and isobaric (*solid line*) ab initio heat capacity at 0 GPa. Acoustic modes contribution has been reported as *dotted grey line*. **b** Three-dimensional plot of isobaric heat at different pressures and in the temperature range 10–900 K

both the energy and geometry of the mineral phase, which also affects other physical–chemical properties. In particular, while *a* and *b* lattice parameters have been accurately simulated in the past by DFT, because they are dominated by strong covalent bonding, the **c** axis length is the most affected by dispersive forces, and prior to the semi-empirical correction for van der Waals forces in quantum mechanics codes, it was generally overestimated by 1.0–1.2 Å (Refson et al. 2003; Sainz-Diaz et al. 2001).

Regarding the vibrational spectrum, we observed that the inclusion of dispersive forces increased anharmonicity of hydroxyl group vibrations and caused a general blue shift of the other modes. These effects can be explained by the reduction of the *c* parameter due to the B3LYP-D* approach. The same conclusion has been drawn in a previous theoretical study on kaolinite, conducted with similar computational approach by Ugliengo et al. (2009). However, the results obtained in the present work on pyrophyllite are encouraging because the most intense signals, even

the anharmonic-corrected OH stretching, are in reasonable agreement with FTIR data on the raw mineral reported in literature (Mukhopadhyay et al. 2010; Ogorodova et al. 2011). Unfortunately, the CRYSTAL09 code does not allow applying the anharmonic correction to other OH vibrational modes, such as librations, and, thus, a proper comparison with experimental data on these signals is limited.

According to our data, pyrophyllite exhibits an anisotropic behaviour, with *a* and *b* lattice parameters less compressible than the *c* one. This is a general observation obtained for almost all phyllosilicates, where the TOT layers are made by covalent bonds and held together by weak interactions. This is in good agreement with previous theoretical and experimental studies conducted on this mineral class (Gatta et al. 2009, 2010, 2013; Pawley et al. 2002; Ulian et al. 2014).

The bulk modulus and its pressure derivative obtained at the athermal limit ($K_{T0} = 48.67$ GPa, $K'_{T0} = 11.14$)

are in quite good agreement with previous theoretical data (Voora et al. 2011), expressing a stiffer structure than the one observed by plane-wave simulations ($K_{T0-DFT-D2} = 38$ GPa, $K'_{T0-DFT-D2} = 11$; $K_{T0-vdW-TS} = 41$ GPa; $K'_{T0-vdW-TS} = 12$). However, it is worth noting that the reported results from the previous simulations are related to the uniaxial compression of pyrophyllite along the **c** axis. The authors considered a series of different c lattice vectors (in the range $c \pm 1.5$ Å) around the equilibrium geometry and then relaxed the atomic positions at constant unit-cell volumes. Thus, the calculated bulk modulus reported by Voora et al. (2011) is an approximation, because the authors neglected the contribution of the **a** axis and **b** axis moduli to the bulk one. For this reason, we compared the results of Voora et al. (2011) only with the c axis modulus, $K_{T0}(c) = 27.74$ GPa and $K'(c) = 8.16$. In this sense, our results show a softer behaviour of pyrophyllite than that obtained by PBE functional corrected for dispersive forces (DFT-D2). This could be due to both the different basis sets and the k sampling along the c lattice direction (two points in the plane-wave simulation, four points in GTO). The study of Voora et al. (2011), like ours, shows the importance of the role of dispersive forces in the calculation of mechanical properties. Indeed, when using standard DFT functionals, the bulk modulus is highly underestimated ($K_{T0-PBE} = 6$ GPa) and the adoption of correction improved the results, depending on both the functional and the quality of the basis set.

We made a comparison between our theoretical results with experimental ones by considering the thermal equation of state and related quantities. We included the thermal effects to the physical–chemical properties of pyrophyllite using the quasi-harmonic approximation, as also done in previous theoretical investigations of different solid phases (Ottonello et al. 2009a; Prencipe et al. 2011; Ulian and Valdrè 2014a, b; Yu and Wentzcovitch 2006).

Our results at $T = 300$ K [$K_T = 46.37(71)$ GPa and $K'_T = 10.51(44)$] are in quite good agreement with those of Pawley et al. (2002), where the authors experimentally obtained $K_T = 37$ GPa and $K'_T = 10$. A very much better agreement was found with the recent study of Gatta et al. (2014), where the authors obtained $K_T = 47(4)$ GPa and $K'_T = 7.3(19)$. We have also a very good agreement of the axial compressibility data from our simulations [$\beta(a) = 3.73 \times 10^{-3}$, $\beta(b) = 3.06 \times 10^{-3}$ and $\beta(c) = 12.8 \times 10^{-}$ GPa^{-1}] with that obtained by experimental means, $\beta(a) = 3.7 \times 10^{-3}$, $\beta(b) = 3.3 \times 10^{-3}$ and $\beta(c) = 13.6 \times 10^{-3}$ GPa^{-1} in the work of Pawley et al. (2002) and $\beta(a) = 3.4 \times 10^{-3}$, $\beta(b) = 3.2 \times 10^{-3}$ and $\beta(c) = 12.8 \times 10^{-3}$ GPa^{-1} in the one of Gatta et al. (2014). More in details, the "linearized" BM3 for axial compressibilities from our simulations corroborates the

results of Gatta et al. (2014): $a_0 = 5.179(3)$ [+0.010] Å, $K_{T0}(a) = 99(6)$ [+10] GPa; $b_0 = 5.184$ Å, $K_{T0}(b) = 104(3)$ [+10] GPa; $c_0 = 9.377(13)$ [+0.009] Å, $K_{T0}(c) = 26(1)$ [+0] GPa (in square brackets, we reported the deviation between theoretical and experimental results). However, the theoretical unit-cell angles showed a slightly different behaviour upon compression. In particular, while the calculated variations of α and γ angles are similar to the experimental ones of Gatta et al. (2014), the β parameter showed a small decrease upon compression up to 3.3 GPa and then increased as experimentally observed. This discrepancy may be explained by the different chemical composition of the two structures: on the one hand, our model is a stoichiometric, defect-free pyrophyllite mineral; on the other hand, the sample investigated by Gatta et al. (2014) presented several atomic substitutions, in particular iron (Fe) atoms in the octahedral sheet and Al atoms in the tetrahedral one.

Regarding the thermal behaviour of pyrophyllite, we noted a deviation between our thermal dependency of the bulk modulus and that of Pawley et al. (2002). At 0 GPa, in the T range 100–900 K, it seems that our model softens more slowly than experimentally observed (-27.6 and -55 bar K^{-1}, respectively). This could be derived from two reasons. First, the thermal behaviour reported by Pawley et al. (2002) is an estimation from several points on a $P–T$ path, whereas we obtained a series of compressional isotherms, $V(P)_T$. Second, while our model can be ascribed as a single-crystal pyrophyllite end-member, the experimental sample was a powder with some substitutional defects (mainly Fe). As previously discussed (Ulian et al. 2014), the quantum mechanical approach based on periodic boundary conditions produces results more similar to single-crystal XRD experiments than X-ray powder diffraction ones. In fact, a very good agreement was found between the theoretical thermal expansion coefficient (α_T) at $T = 300$ K ($\alpha_T = 1.8 \times 10^5$ K^{-1}) and the one experimentally obtained by Gatta et al. (2014) ($\alpha_T = 2.2(2) \times 10^5$ K^{-1}) by single-crystal synchrotron XRD.

References

Alimdzhanova DI, Ismatov AA, Ganieva MM (1999) The effect of quartz-pyrophyllite raw material on porcelain structure formation. Glass Ceram 56:61–63

Anderson OL (1995) Equation of state of solids for geophysics and ceramic science. Oxford University Press, New York, p 405

Angel RJ (2001) EOS-FIT6.0. Computer program (http://www.ros-sangel.com)

Bailey SW (1988) Introduction, hydrous phyllosilicates. Rev Mineral Geochem 19:1–8

Becke AD (1993) Density-functional thermochemistry. 3. The role of exact exchange. J Chem Phys 98:5648–5652

Bhasin S, Amritphale SS, Chandra N (2003) Effect of pyrophyllite additions on sintering characteristics of fly ash based ceramic wall tiles. Br Ceram Trans 102:83–86

Birch F (1947) Finite elastic strain of cubic crystal. Phys Rev 71:809–824

Broyden CG (1970a) The convergence of a class of double-rank minimization algorithms 1. General considerations. IMA J Appl Math 6:76–90

Broyden CG (1970b) The convergence of a class of double-rank minimization algorithms: 2. The new algorithm. IMA J Appl Math 6:222–231

Bruno M, Prencipe M, Valdrè G (2006) Ab initio quantum-mechanical modeling of pyrophyllite Al2Si4O10(OH)(2) and talc Mg3Si4O10(OH)(2) surfaces. Phys Chem Miner 33:63–71

Catti M, Valerio G, Dovesi R, Causa M (1994) Quantum-mechanical calculation of the solid-state equilibrium MgO + alpha-Al$_2$O$_3$ MgAl$_2$O$_4$ (spinel) versus pressure. Phys Rev B 49:14179–14187

Civalleri B, Zicovich-Wilson CM, Valenzano L, Ugliengo P (2008) B3LYP augmented with an empirical dispersion term (B3LYP-D*) as applied to molecular crystals. CrystEngComm 10:405–410

Dovesi R, Saunders VR, Roetti C, Orlando R, Zicovich-Wilson CM, Pascale F, Civalleri B, Doll K, Harrison NM, Bush IJ, D'Arco P, Llunell M (2009) CRYSTAL09 user's manual. University of Torino, Torino

Evans BW, Guggenheim S (1988) Talc, pyrophyllite, and related minerals. Rev Miner 19:225–294

Fletcher R (1970) A new approach to variable metric algorithms. Comput J 13:317–322

Gatta GD, Rotiroti N, Pavese A, Lotti P, Curetti N (2009) Structural evolution of a 3T phengite mica up to 10 GPa: an in situ single-crystal X-ray diffraction study. Z Krist 224:302–310

Gatta GD, Rotiroti N, Lotti P, Pavese A, Curetti N (2010) Structural evolution of a 2 M (1) phengite mica up to 11 GPa: an in situ single-crystal X-ray diffraction study. Phys Chem Miner 37:581–591

Gatta GD, Merlini M, Valdrè G, Liermann H-P, Nenert G, Rothkirch A, Kahlenberg V, Pavese A (2013) On the crystal structure and compressional behavior of talc: a mineral of interest in petrology and material science. Phys Chem Miner 40:145–156

Gatta GD, Lotti P, Merlini M, Liermann H-P, Lausi A, Valdrè G, Pavese A (2014) Elastic behaviour and phase stability of pyrophyllite and talc at high pressure and temperature. Phys Chem Miner. doi:10.1007/s00269-014-0721-x

Goldfarb D (1970) A family of variable-metric methods derived by variational means. Math Comput 24:23–26

Grimme S (2006) Semiempirical GGA-type density functional constructed with a long-range dispersion correction. J Comput Chem 27:1787–1799

Grove TL, Till CB, Krawczynski MJ (2012) The role of H$_2$O in subduction zone magmatism. In: Jeanloz R (ed) Annual review of earth and planetary sciences. Annual Reviews, Palo Alto, pp 413–439

Haas JL, Fisher JR (1976) Simultaneous evaluation and correlation of thermodynamic data. Am J Sci 276:525–545

Holland TJB, Powell R (1998) An internally consistent thermodynamic data set for phases of petrological interest. J Metamorph Geol 16:309–343

Kieffer SW (1979a) Thermodynamics and lattice vibrations of minerals—1. Mineral heat capacities and their relationships to simple lattice vibrational models. Rev Geophys Space Phys 17:1–19

Kieffer SW (1979b) Thermodynamics and lattice vibrations of minerals—2. Vibrational characteristics of silicates. Rev Geophys Space Phys 17:20–34

Kieffer SW (1979c) Thermodynamics and lattice vibrations of minerals—3. Lattice dynamics and an approximation for minerals with application to simple substances and framework of silicates. Rev Geophys Space Phys 17:35–59

Krupka KM, Robie RA, Hemingway BS (1979) High-temperature heat capacities of corundum, periclase, anorthite, CaAl$_2$Si$_2$O$_8$

glass, muscovite, pyrophyllite, KAlSi$_3$O$_8$ glass, grossular, and NaAlSi$_3$O$_8$ glass. Am Mineral 64:86–101

Lee JH, Guggenheim S (1981) Single-crystal X-Ray refinement of pyrophyllite-1Tc. Am Mineral 66:350–357

Lee CT, Yang WT, Parr RG (1988) Development of the Colle-Salvetti correlation-energy formula into a functional of the electron-density. Phys Rev B 37:785–789

Lintz EH (1938) Use of talc and pyrophyllite in semi-vitreous dinnerware bodies. J Am Ceram Soc 21:229–237

Mazo MA, Manevitch LI, Gusarova EB, Berlin AA, Balabaev NK, Rutledge GC (2008) Molecular dynamics simulation of thermomechanical properties of montmorillonite crystal. II. Hydrated montmorillonite crystal. J Phys Chem C 112:17056–17062

Momma K, Izumi F (2008) VESTA: a three-dimensional visualization system for electronic and structural analysis. J Appl Crystallogr 41:653–658

Monkhorst HJ, Pack JD (1976) Special points for Brillouin-zone integrations. Phys Rev B 8:5188–5192

Mukhopadhyay TK, Ghatak S, Maiti HS (2010) Pyrophyllite as raw material for ceramic applications in the perspective of its pyrochemical properties. Ceram Int 36:909–916

Mukhopadhyay TK, Dana K, Ghatak S (2011) Pyrophyllite—a potential material for application in tri-axial porcelain systems. Ind Ceram 31:165–173

Murnaghan FD (1937) Finite deformations of an elastic solid. Am J Math 49:235–260

Ogorodova LP, Kiseleva IA, Mel'chakova LV, Vigasina MF, Spiridonov EM (2011) Calorimetric determination of the enthalpy of formation for pyrophyllite. Russ J Phys Chem A 85:1492–1494

Ottonello G, Civalleri B, Ganguly J, Zuccolini MV, Noel Y (2009a) Thermophysical properties of the α–β–γ polymorphs of Mg2SiO4: a computational study. Phys Chem Miner 36:87–106

Ottonello G, Zuccolini MV, Civalleri B (2009b) Thermo-chemical and thermo-physical properties of stishovite: an ab initio all-electron investigation. Calphad 33:457–468

Ottonello G, Civalleri B, Ganguly J, Perger WF, Belmonte D, Zuccolini MV (2010) Thermo-chemical and thermo-physical properties of the high-pressure phase anhydrous B (Mg$_{14}$Si$_5$O$_{24}$): an ab initio all-electron investigation. Am Mineral 95:563–573

Pascale F, Zicovich-Wilson CM, Gejo FL, Civalleri B, Orlando R, Dovesi R (2004) The calculation of the vibrational frequencies of crystalline compounds and its implementation in the CRYSTAL code. J Comput Chem 25:888–897

Pawley AR, Clark SM, Chinnery NJ (2002) Equation of state measurements of chlorite, pyrophyllite, and talc. Am Mineral 87:1172–1182

Perger WF, Criswell J, Civalleri B, Dovesi R (2009) Ab-initio calculation of elastic constants of crystalline systems with the CRYSTAL code. Comput Phys Commun 180:1753–1759

Prencipe M, Pascale F, Zicovich-Wilson CM, Saunders VR, Orlando R, Dovesi R (2004) The vibrational spectrum of calcite (CaCO$_3$): an ab initio quantum-mechanical calculation. Phys Chem Miner 31:559–564

Prencipe M, Scanavino I, Nestola F, Merlini M, Civalleri B, Bruno M, Dovesi R (2011) High-pressure thermo-elastic properties of beryl (Al$_4$Be$_6$Si$_{12}$O$_{36}$) from ab initio calculations, and observations about the source of thermal expansion. Phys Chem Miner 38:223–239

Refson K, Park SH, Sposito G (2003) Ab initio computational crystallography of 2:1 clay minerals: 1. Pyrophyllite-1Tc. J Phys Chem B 107:13376–13383

Robie RA, Hemingway BS, Wilson WH (1976) Heat capacities of calorimetry conference copper and of muscovile KAl$_2$(AlSi$_3$)O$_{10}$(OH)$_2$, pyrophyllite Al$_2$Si$_4$O$_{10}$(OH)$_2$, and illite K$_3$(Al$_7$Mg)(Si$_{14}$Al$_2$)O$_{40}$(OH)$_8$ between 15 and 375 K and their standard entropies at 298.15K. J Res US Geol Surv 4:631–644

Sainz-Diaz CI, Hernandez-Laguna A, Dove MT (2001) Modeling of dioctahedral 2:1 phyllosilicates by means of transferable empirical potentials. Phys Chem Miner 28:130–141

Shanno DF (1970) Conditioning of quasi-Newton methods for function minimization. Math Comput 24:647–656

Sobolev AV, Chaussidon M (1996) H_2O concentrations in primary melts from supra-subduction zones and mid-ocean ridges: implications for H_2O storage and recycling in the mantle. Earth Planet Sci Lett 137:45–55

Stixrude L (2002) Talc under tension and compression: spinodal instability, elasticity, and structure. J Geophys Res Solid Earth 107

Tosoni S, Pascale F, Ugliengo P, Orlando R, Saunders VR, Dovesi R (2005) Quantum mechanical calculation of the OH vibrational frequency in crystalline solids. Mol Phys 103:2549–2558

Tunega D, Bucko T, Zaoui A (2012) Assessment of ten DFT methods in predicting structures of sheet silicates: importance of dispersion corrections. J Chem Phys 137

Ugliengo P, Viterbo D, Chiari G (1993) MOLDRAW: molecular graphic on a personal computer. Z Krist 207:9–23

Ugliengo P, Zicovich-Wilson CM, Tosoni S, Civalleri B (2009) Role of dispersive interactions in layered materials: a periodic B3LYP and B3LYP-D* study of Mg(OH)(2), Ca(OH)(2) and kaolinite. J Mater Chem 19:2564–2572

Ulian G, Valdrè G (2014a) Density functional investigation of the thermo-physical and thermo-chemical properties of $2M_1$ muscovite. Am Mineral 2015. doi:10.2138/am-2015-5086

Ulian G, Valdrè G (2014b) Density functional investigation of the thermophysical and thermochemical properties of talc [$Mg_3Si_4O_{10}(OH)_2$]. Phys Chem Miner 2015. doi:10.1007/s00269-014-0708-7

Ulian G, Tosoni S, Valdrè G (2013) Comparison between Gaussian-type orbitals and plane wave ab initio DFT modeling of layered silicates: talc mineral as model system. J Chem Phys 139:204101

Ulian G, Tosoni S, Valdrè G (2014) The compressional behaviour and the mechanical properties of talc [$Mg_3Si_4O_{10}(OH)_2$]: a density functional theory investigation. Phys Chem Miner 41:639–650

Voora VK, Al-Saidi WA, Jordan KD (2011) Density functional theory study of pyrophyllite and M-montmorillonites (M = Li, Na, K, Mg, and Ca): role of dispersion interactions. J Phys Chem A 115:9695–9703

Wardle R, Brindley GW (1972) The crystal structure of pyrophyllite, 1Tc, and of its dehydroxylate. Am Mineral 57:732–750

Yu YGG, Wentzcovitch RM (2006) Density functional study of vibrational and thermodynamic properties of ringwoodite. J Geophys Res Solid Earth 111